Supporting information

S1. Layer de-Convolution Williamson-Hall method (LdCWH)

S.1.1. Theoretical background and uncertainties determination

ω-scans consist in scans through an ellipsoidal-arc in the reciprocal space, while keeping the detector fixed. 2θ-ω scans, on the other hand, correspond to a cut in the reciprocal space connecting (Q_x,Q_z) coordinate of the Bragg peak centroid with the origin of the reciprocal space $(Q_x,Q_z)=(0,0)$. In the particular case of symmetrical reflections, the Bragg angular position corresponds to $\omega_B=2\theta_B/2$. ω-scans are sensitive to the coherence length parallel to the substrate surface ($L_{\parallel}$) and to the tilt angle ($^{\alpha_\theta}$) while 2θ-ω scans are sensitive to the coherence length perpendicular to the substrate surface ($^{L_\perp}$) and to the heterogeneous strain ($^{\varepsilon_\perp}$) also perpendicular to the substrate surface. Analytically, the coherence length parallel (perpendicular) to the substrate surface and the tilt angle (heterogeneous strain) are given by Eqs. S.1a) and b), respectively[1,2]:

$$L_{\parallel(\perp)} = \frac{0{,}9 \cdot \lambda}{\beta_{\theta(2\theta-\omega)}\left[0.017475 + 1.500484 \cdot a_3 - 0.534156 \cdot a_3^2\right] \cdot sin(cos)\left(\theta_{B(000l)}\right)} \Leftrightarrow L_{\parallel(\perp)} = \frac{0.9 \cdot \lambda}{\beta_{\theta(2\theta-\omega)} \cdot \mu \cdot sin(cos)\left(\theta_{B(000l)}\right)} \quad \text{Eq. S.1a)}$$

$$\alpha_\theta(\varepsilon_\perp) = \frac{\beta_{\theta(2\theta-\omega)}\left[0.184446 + 0.812692 \cdot \left(1 - 0.998497 \cdot a_3\right)^{\frac{1}{2}} - 0.65960\right.}{\left(4tan(\theta_B)\right)} \quad \text{Eq. S.1b)}$$

$$(\varepsilon_\perp) = \beta_{\theta(2\theta-\omega)} \cdot \rho$$

$$\beta_{\theta(2\theta-\omega)} = \left(a_3 \cdot \pi + (1 - a_3)\sqrt{\pi \cdot ln(2)}\right) \cdot \frac{FWHM}{2} \quad \text{Eq. S.1c)}$$

$$I(\theta(2\theta-\omega)) = a_0 \times \left[(1 - a_3) \times exp\left(-log(2) \times \left(\frac{\theta(2\theta) - a_1}{a_2}\right)^2\right) + \frac{a_3}{1 + \left(\frac{\theta(2\theta) - a_1}{a_2}\right)^2}\right] \quad \text{Eq. S.1d)}$$

$L_{\parallel(\perp)}$ refers to parallel (perpendicular) coherence length, $\beta_{\theta(2\theta-\omega)}$ to ω or 2θ-ω scan integral breadth (Eq. S.1c) and generically defined as the ratio between the peak area and peak maximum[3] and $\alpha_\theta(\varepsilon_\perp)$ to the tilt angle (heterogeneous strain), respectively. Moreover, for the case of the heterogeneous strain it increases proportionally to $1/\left(4tan(\theta_B)\right)$. λ is the Cu $k\alpha_1$ X-ray wavelength (1.54056 Å), θ_B is the Bragg angle and (000l) is the measured reflection. μ and ρ compress the polynomials in brackets, which are functions of the Lorentzian fraction, a_3. a_2 is

the Gaussian width which is half of the FWHM, a_1 is the PV center, a_0 is the intensity maximum and I(θ(2θ-ω)) represents the intensity for given incident angle, $\theta(2\theta)$. The Pseudo-Voigt definition used in this work is defined in Eq. S.1d). With respect of Eq. S1.d) special attention is needed because it is an approximation valid for low backgrounds and single peaks. Mathematically, if the coefficients of three PVs are independent, then, based on the central limit theorem, the sum of three PVs is still a PV. On the other hand, the sum of the $\beta_{\theta(2\theta-\omega)}$ using Eq. S.1d) only approximates the integral breadth definition - ratio between the peak area and peak maximum - if the background of the measured curve can be neglected compared to the maximum intensity. In fact, all measured curves were simulated with low backgrounds due to the fact that measurements were performed in high-resolution mode. Moreover, if $\beta^{asymmetric\ peak}_{\theta(2\theta-\omega)} > \beta^{PV1}_{\theta(2\theta-\omega)}$, which is true by definition (PV(i=1) is the Pseudo-Voigt function that characterizes the major slab and $\beta^{asymmetric\ peak}_{\theta(2\theta-\omega)}$ is the integral breadth of the total measured curve), then $\beta^{PVi\ (i=2,3)}_{\theta(2\theta-\omega)}$, which characterizes the remaining layers integral breadths can be de-convoluted in several different ways not limiting the usage of Eq. S.1c) to obtain the integral breadth for the thicker slab. The distribution of the intensities among the other two layers can be calculated to fulfill the condition of having the summation of the partial $\beta_{\theta(2\theta-\omega)}$ to approximate with the integral breadth definition for the total asymmetric peak. To conclude, due to the fact that LdCWH method is directly applied only to the thicker slab in this manuscript, in fact a possible quantification of the corresponding integral breadth is, indeed, the one found using Eq. S1.c). To obtain the uncertainties of $L_{\parallel}$ and α_θ, an understanding of the FWHM, Gaussian width and integral breadth relations are fundamental due to the fact that, according to Eq. S.1a) to S.1c), these are independent quantities. Figures S.1a) and b) show the evolution of the ρ and μ (terms in brackets from Eq S.1a) and S.1b)) plotted together with the integral breadth for the FWHMs of 0.01 °, 0.1 ° and 0.25 ° as functions of a_3 coefficient of the PV. It is verified that the integral breadth is a linear increasing function of a_3 coefficient of the PV and that the terms ρ and μ from equations S.1a) and S.1b) decrease and increase with a_3, respectively. Moreover, the increase in $\frac{\partial \rho}{\partial a_3}$ and $\frac{\partial \mu}{\partial a_3}$ is higher than $\frac{\partial \beta_{\theta(2\theta-\omega)}}{\partial a_3}$ and $\frac{\partial \beta_{\theta(2\theta-\omega)}}{\partial a_3}$ for FWHMs of 0.01º, 0.1º and 0.25º, the typical FWHMs in the case of nitride compounds. These differences imply that, in the case of figure S.1b), the decrease/increase of component a_3 from the PV forces the product of $\beta_\theta \cdot \rho$ to increase/decrease, thereby increasing/decreasing the crystallites tilt angle. Nevertheless, in the particular case of a_3=0, i. e., a pure Gaussian, ρ is maximized, thus, so is the tilt angle. On the other hand, if a_3 is 1, corresponding to a pure Lorentzian, μ is maximum (close to unity), therefore, $L_{\parallel}$ matches its minimum (figure S.1b).

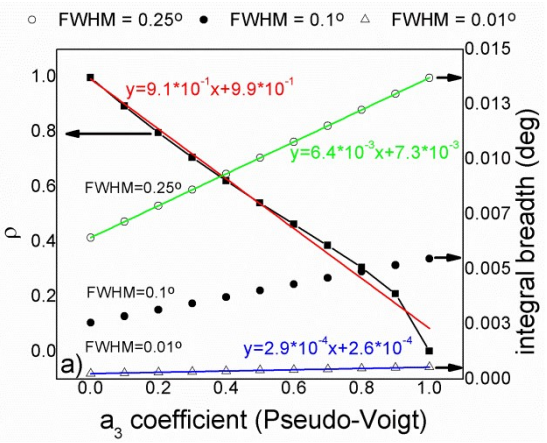

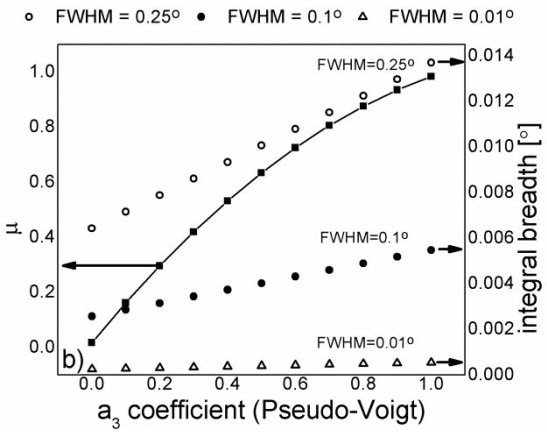

Figure S1 Evolution of the terms ρ (a), and μ (b) from Eq. S.1a) and S.1b), as functions of a_3 component of the Pseudo Voigt. Likewise, integral breadths for three different FWHM (0.01º, 0.1º and 0.25º) as functions of a_3 component of the PV are shown. The selected choices for the FWHM correspond to the typical FWHM found in the AlGaN compounds.

The uncertainties of $L_{\parallel}$ and $^{\alpha_\theta}$ are, then, found through the propagation of errors and using the uncertainties derived for each 0002, 0004 and 0006 ω-scans Pseudo-Voigt fittings. With respect to $L_{\parallel}$ the highest uncertainty is due to the error at the a_3 coefficient of the Pseudo-Voigt fitting. $\left(\frac{\partial L_{\parallel}}{\partial a_3}\cdot \Delta a_3\right)^2 \equiv I_1$ is approximately three orders of magnitude greater than the uncertainty at the FWHM, $\left(\frac{\partial L_{\parallel}}{\partial FWHM}\cdot \Delta FWHM\right)^2 \equiv I_2$. Furthermore, the uncertainties at the Pseudo-Voigt center and X-ray wavelength can be neglected compared to I_1 an I_2, respectively. Related to the crystallites tilt angle, $^{\alpha_\theta}$, the only independent quantities are a_3 and FWHM. $\left(\frac{\partial \alpha_\theta}{\partial a_3}\cdot \Delta a_3\right)^2$ is two orders of magnitude greater than $\left(\frac{\partial \alpha_\theta}{\partial FWHM}\cdot \Delta FWHM\right)^2$. On the other hand, the y-axis at the standard WH plot is given by the product between the scattering vector length, sin(θ)/λ, and the integral breadth, β_θ. Basically, the WH plot relies on the principle that size broadening parallel component ($\frac{K\lambda}{L_{||}sin(\theta_B)}$), and perpendicular component ($\frac{K\lambda}{L_{\perp}sin(\theta_B)}$), tilt angle ($\beta_\theta$) and strain broadening ($C\varepsilon tan(\theta_B)$) as functions of the Bragg angle varies significantly. K is considered to be 0.9 in this work and C=4. Assuming the sum of size and strain broadenings in the total broadening results in $\frac{\beta_\theta sin(\theta_B)}{\lambda} = \frac{0.9}{2y_0^{\omega}} + m^{\omega}$ and $\frac{\beta_\theta cos(\theta_B)}{\lambda} = \frac{0.9}{2y_0^{2\theta-\omega}} + m^{2\theta-\omega}$, where $y_0^i (i = \omega, 2\theta-\omega)$ is the y-intercept and $m^i (i = \omega, 2\theta-\omega)$ is the slope for the ω and 2θ-ω scans, respectively. The uncertainties derived in the case of the standard Williamson-Hall method are given by:

$$\Delta y_{\beta_{\theta(FWHM)}} = \sqrt{\left(\frac{sin(\theta_B)}{\lambda}\Delta\beta_\theta(FWHM)\right)^2 + \left(\frac{\beta_\theta(FWHM)cos(\theta_B)}{\lambda}\Delta\theta_B\right)^2} \qquad \text{Eq. S.1.2}$$

where the values in brackets to use correspond to the integral breadth (β_θ) or FWHM, respectively. $\Delta\beta_\theta(FWHM)$ is the uncertainty of integral breadth (FWHM). The uncertainty at β_θ is calculated applying the propagation of errors to Eq. S.1c). ΔFWHM and Δa_3 are the uncertainties at the FWHM and at the Lorentzian fraction and are determined directly via the PV fitting. The uncertainty $\left(\frac{\partial \beta_\theta}{\partial FWHM}\cdot \Delta FWHM\right)^2$ is around one order of magnitude greater than $\left(\frac{\partial \beta_\theta}{\partial a_3}\cdot \Delta a_3\right)^2$. $\Delta\theta_B$ is the uncertainty of the Bragg peak center, i. e., the a_1 coefficient of PV1.

S2. Procedure to speed up LdCWH fitting convergence

A method to accelerate the convergence for linearity is described. It starts with the independent fitting of the lower Miller index reflection using three PVs. By "independent" fitting depicted as step I on the flowchart (figure 2 of manuscript), the authors mean that reflection 0002 is fitted without any concern about the remaining ones. The 0002 ω-scan Pseudo Voigt 1 (PV1) is defined according to its a_0 (intensity), a_1 (center), a_2 (Gaussian width) and a_3 (Lorentzian fraction) coefficients, and then PV2 and PV3 are included in the simulations as appropriate. The a_3 components of PV2 and PV3 are calculated in a way that $L_{\parallel}$ is the closest to the one derived for the 0002 ω-scans: first, steps of 0.01 in a_3 are given as input in Eq. S.1a) and $L_{||}$ derived for 0004 and 0006 are calculated. In this case, as shown in figure 4a), #iteration 3 is found for both reflections which translates into a_3 0004 of 0.09 and 0.23 for a_3 0006 from the given starting a_3. This is the evidence that the size effect broadening in the reciprocal space is independent of the scattering vector length as it is possible to obtain similar $L_{||}$ independently of the reflection. The straight line in figure S2.1a) corresponds to the $L_{\parallel}$ derived for 0002. On the other hand, it is not possible to calculate a_3 in a way that α_θ derived for 0004 and 0006 is close to the one derived for 0002 as concluded from figures S2.1c) and S2.1d). The horizontal line corresponds to the α_θ derived for 0002. Although iterations #164 and #169 are rejected based on the fact that, by definition, $0 \leq a_3 \leq 1$, there isn't any possible iteration that matches the horizontal line in figure S.2.1c) with any of the curves derived for incremental a_3 in the case of α_θ using Eq. S.2.1b) for 0004 and 0006, simultaneously. The procedure, represented in figures 4a-d), enables to speed up the fitting convergence process.

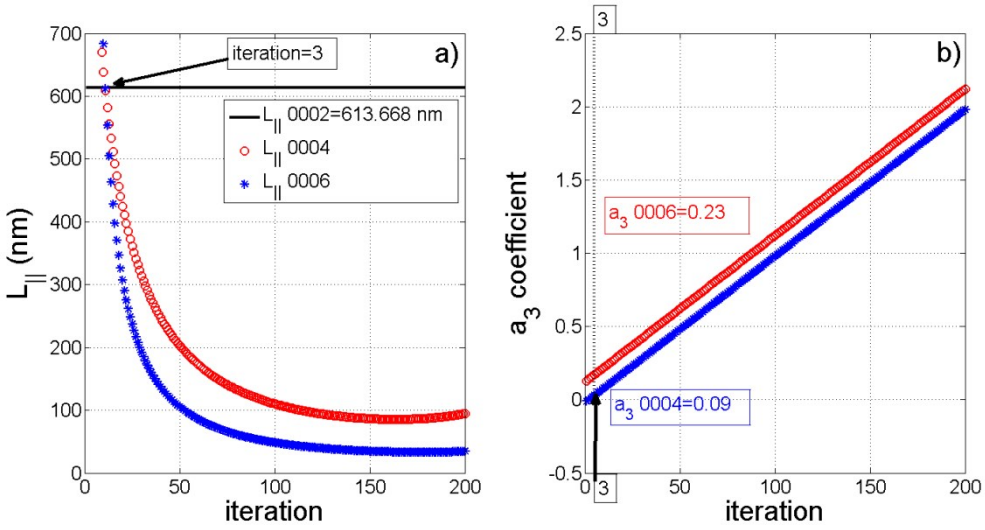

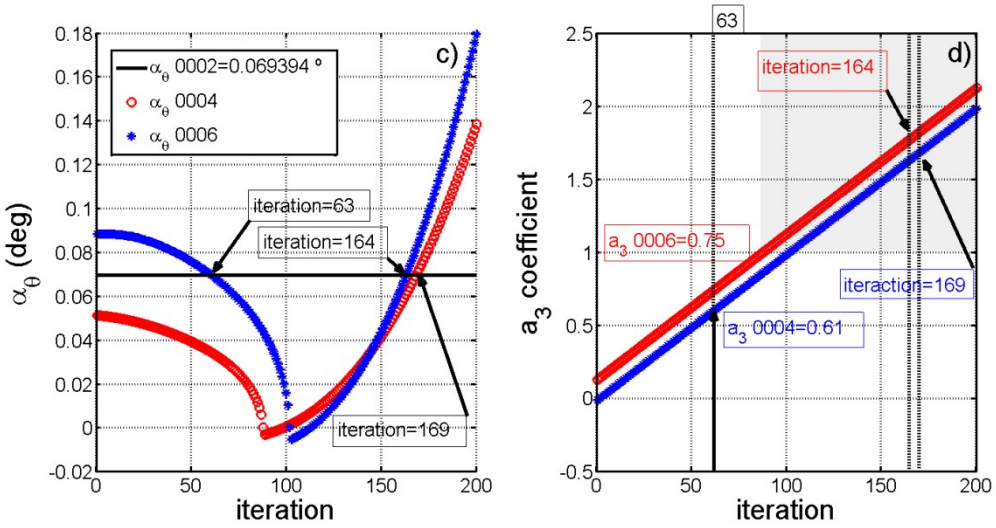

Figure S2 a) Comparison between the theoretical $L_{\parallel}$ determined using steps of 0.01 in a_3 (Lorentzian fraction) for the 0004 and 0006 with the 0002 derived $L_{\parallel}$ (horizontal line). Iteration #3 corresponds to the intersection between the derived lateral coherence lengths for the three reflections. b) Determination of the corresponding a_3 for 0004 and 0006 which outputs the closest possible $L_{\parallel}$ determined for 0002. c-d) Same as for a-b) but with respect to the α_θ. Iteration #63 matches derived 0006 and 0002 α_θ which corresponds to a_3 0006=0.61 but there isn't any possible combination within $0 \leq a_3 \leq 1$ for matching derived 0002 and 0004 α_θ. Shadowed area in d) corresponds to not allowed a_3 range because, by definition, $0 \leq a_3 \leq 1$.

S3. Multiple Reflection optimization package for X-ray diffraction

Figure S3 a-c) show experimental 2θ-ω around the $02\bar{2}0$, $04\bar{4}0$ and $06\bar{6}0$ α-MoO_3 Bragg peaks and respective simulations using the dynamical theory of X-ray diffraction.

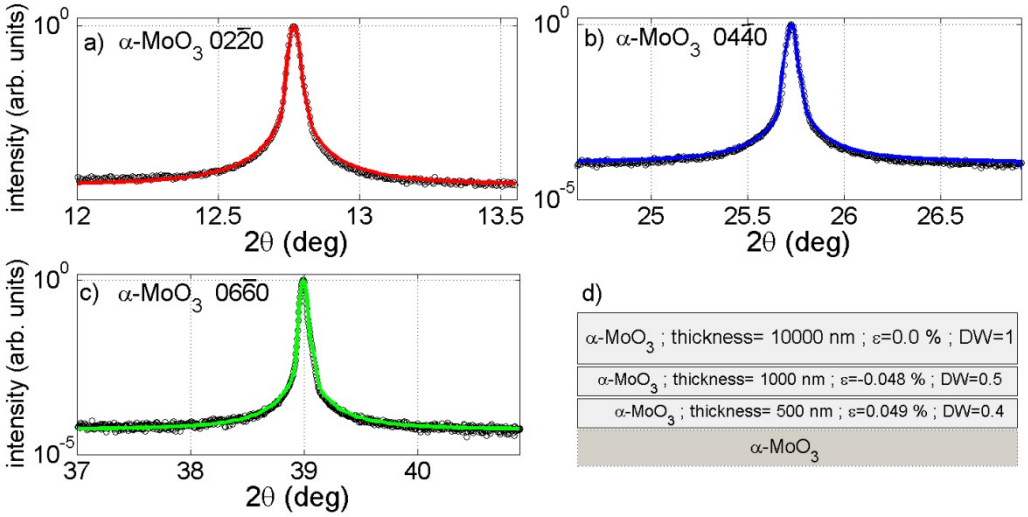

Figure S3 a-c) Experimental and simulation of the 2θ-ω scans around the vicinity of the $02\bar{2}0$, $04\bar{4}0$ and $06\bar{6}0$ α-MoO_3 Bragg peaks. The simultaneous simulations and fittings were accomplished using the MROX code[4-6]. d) Schematics of the top α-MoO_3 surface layers with the corresponding layer thickness, deformation perpendicular to the sample surface and crystalline quality.

All software was developed under Matlab® Graphical User Interface Development Environment (GUIDE). LdCWH software is available via email upon request.

References

[1] Th. de Keijser, E. J. Mittemeijer and H. C. F. Rozendaal, *J. Appl. Crystallogr.*, 1983, 16, 309-316.

[2] T. Metzger, R. Hopler, E. Born, O. Ambacher, M. Stutzmann, R. Stommer, M. Schuster, H. Gobel, S. Christiansen, M. Albrecht and H. P. Strunk, *Philos. Mag. A*, 1998, 77(4), 1013-1025.

[3] M. Birkholz, P. Fewster and C. Genzel, *Mater. Charact.*, 2005, 58(3) 318.

[4] S. Magalhaes, M. Fialho, M. Peres, K. Lorenz and E. Alves, *J. Phys. D: Applied Physics*, 2016, 49(13), 135308.

[5] P. Jozwik, S. Magalhaes, R. Ratajczak, C. Mieszczynski, M. Sequeira, A. Turos, R. Bottger, R. Heller, K. Lorenz and E. Alves, *Phys. Status Solidi B*, 2019, 256(5), 1800364.

[6] M. Fialho, S. Magalhaes, J. Rodrigues, M. P. Chauvat, P. Ruterana, T. Monteiro, K. Lorenz, E. Alves, *Surf. Coat. Technol.*, 2018, 355, 29-39.